ELSEVIER

www.elsevier.nl/locate/jelechem

Journal of Electroanalytical Chemistry 489 (2000) 55–67

Journal of Electroanalytical Chemistry

In situ investigation of electrochemical lithium intercalation into graphite powder

Chunsheng Wang [a,*], Imran Kakwan [a], A. John Appleby [a], Frank E. Little [b]

[a] *Center for Electrochemical Systems and Hydrogen Research, Texas Engineering Experiment Station, Texas A&M University, College Station, TX 77843-3118, USA*

[b] *Center for Space Power, Texas Engineering Experiment Station, Texas A&M University, College Station, TX 77843-3118, USA*

Received 22 November 1999; received in revised form 17 April 2000; accepted 9 May 2000

Abstract

The reaction kinetics for the electrochemical insertion–extraction of lithium into and out of graphite and the electrode intrinsic resistance have been studied using galvanostatic intermittent titration with applied microcurrent pulses (GIT), electrochemical impedance spectroscopy (EIS) and in situ intrinsic (i.e. physical) resistance measurements. The formation of a so-called solid electrolyte interphase (SEI) or 'passivation layer' on the graphite surface at about +0.8 V versus Li^+/Li increases the total intrinsic resistance within the electrode on the first cycle. The gradual growth (i.e. change in volume) of the SEI film during repeated lithium insertion–extraction results in a continued increase in intrinsic resistance. The good agreement between EIS and in situ intrinsic resistance measurements indicates that the latter is a simple and powerful method for investigating the change in this parameter for graphite electrodes. GIT showed a gradual increase in kinetic rate in an initial single-phase region, followed by a decrease in a two-phase transformation region, which was in turn followed by an increase in kinetic rate in a second single-phase region. This is explained by a shrinking unreacted core model. The controlling step of lithium insertion–extraction during the two-phase transformation region was investigated by EIS and GIT.

Keywords: Electrochemical reaction kinetics; Intrinsic resistance; Electrochemical impedance spectroscopy

1. Introduction

Graphites are extensively used as secondary lithium-ion battery anodes because of their high practical energy density, charge–discharge reversibility, non-toxicity, safety, and cost. Their reversible and irreversible capacity, rate capability and cycling capability characteristics determine their utility.

It is generally accepted that reversible lithium charging capacities of graphite depends on their structural characteristics. Their irreversible capacities and long-term cycling capability largely depend on the amount of particle disintegration resulting from expansion/contraction during lithium insertion and extraction and on the relative stability of passivating surface films, which are commonly referred to as a 'solid electrolyte interphase' (SEI) [1]. The SEI forms from solvent molecules when the double layer potential difference reaches a critical value, and it covers all the electrode surface exposed to the electrolyte. It must be permeable to Li^+ cations to permit reaction, but must also be an electronic insulator to prevent further electrolyte decomposition. Hence, both the formation of SEI films on individual graphite particles, and the gradual disintegration of these particles, will influence the overall conductivity of the graphite electrode. In situ monitoring of electrode conductivity is important for understanding the long-term cycling capability of graphite electrodes. Nishizawa et al. [2] have studied the in situ change in conductivity of a single mesocarbon microbead (MCMB) particles and SEI films on MCMBs using cyclic voltammetry (CV) and microelectrode-based methods. They found that the conductivity and redox activity of MCMB SEI films decreased on continued CV cycling, while these parameters remain stable on individual MCMB particles. The resistance (or conductivity) measured by dc methods is the total intrinsic

* Corresponding author. Fax: +1-979-8459287.
E-mail address: cswang@pop.tamu.edu (C. Wang).

0022-0728/00/$ - see front matter
PII: S0022-0728(00)00197-2

Table 1
Nominal particle sizes and BET surface areas of graphite powders

Sample	Nominal particle size/μm	BET surface area/m^2 g^{-1}	Distributor
Timrex KS 15	15	12	Timcal A.G.
MCMB 10-28	10	1.5	Osaka Chemical Co.
JM 287	<15	13.5	Johnson Matthey

or physical resistance resulting from the ionic conduction of SEI films and the electronic interconnection resistance between carbon particles themselves and their current collector contacts. As the authors state, the results obtained by CV cannot be quantitatively compared with those obtained by constant-current potentiometry, which has been frequently used for lithium-ion battery characterization. Finally, the faradaic reaction current may also interfere with the intrinsic conductivity measured.

Microperturbation techniques such as electrochemical impedance spectroscopy (EIS) and galvanostatic intermittent titration with applied microcurrent pulses (GIT, i.e. galvanostatic microdischarge as a function of state-of-charge, SOC), are effective for the determination of impedances or rates of individual electrode kinetic processes [3]. EIS can give the individual resistances for each reaction step if their time constants are resolvable [4]. GIT can give the equilibrium potential and total reaction resistance of lithium insertion–extraction as a function of lithium content if the pulsed current is small and the relaxation time is sufficiently long for the equilibrium potential to be attained [5]. In this work, the kinetics and cycling stability of graphite electrodes have been studied by using in situ intrinsic (i.e. physical) resistance measurements, EIS, and GIT. The reaction resistances and intrinsic resistances measured using EIS and GIT as a function of lithium content are compared.

2. Experimental

2.1. Electrode and cell preparation

Three graphite powder samples (MCMB 10-28, KS 15, and JM 287) were used as anode materials. Their nominal particle size, BET surface area, and source are shown in Table 1.

Electrodes consisted of 92 wt.% graphite powder and 8 wt.% polyvinylidene fluoride (Kynar™, Elf-Atochem) in 1-methyl-2-pyrrolidinone solvent. After drying overnight at 120°C, they were pressed between two Ni mesh current collectors into a sandwich structure with a geometric area of 2.0 cm^2 containing ca. 50 mg of active graphite (Fig. 1). Electrochemical measurements were performed in a three-compartment PTFE cell of conventional design, with lithium foil counter and reference electrodes. Potentials are given versus this reference electrode in the electrolyte used, 1.0 M $LiPF_6$ in a 1:1:3 by volume ethylene carbonate (EC)–propylene carbonate (PC)–dimethylcarbonate (DMC) mixture (High Purity Lithium Battery Grade, Mitsubishi Chemical Company). Cells were assembled in an argon-filled glove box. Charge (lithium intercalation) and discharge (lithium extraction) characteristics were measured between + 0.0 and + 1.5 V at a constant current using an Arbin Corporation (College Station, TX) automatic battery cycler.

2.2. In situ intrinsic resistance measurement

The in situ intrinsic resistance measurement is shown in Fig. 1. Two potentiostats were used, one for electrochemical lithium insertion–extraction to and from the electrode, the other for measuring intrinsic resistance by application of constant current (10 mA for JM 287, 5 mA for KS 15, and 1 mA for the low bulk density MCMB 10-28 electrodes, chosen to give less than 10 mV between the two outer current collectors).

To avoid confusion over the various electrode resistances discussed here, the expression intrinsic resistance is used below to refer to those physical elements of resistance that are present within the thickness of the electrode, excluding any electrochemical (faradaic) elements. These include the electronic resistance of the series-parallel array of graphite particles themselves, the transmission line of contact resistances between the particles, ionic (electrolytic) contacts, and the electronic resistances of the current collectors and the contact resistances between them and the neighboring graphite particles. This intrinsic resistance may be evaluated by an in situ direct current method.

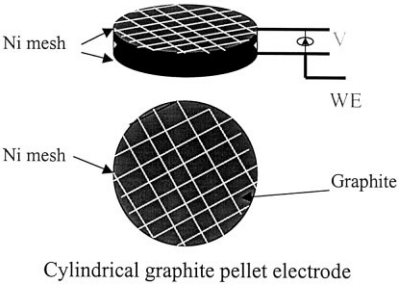

Fig. 1. Schematic diagram of graphite electrode configuration.

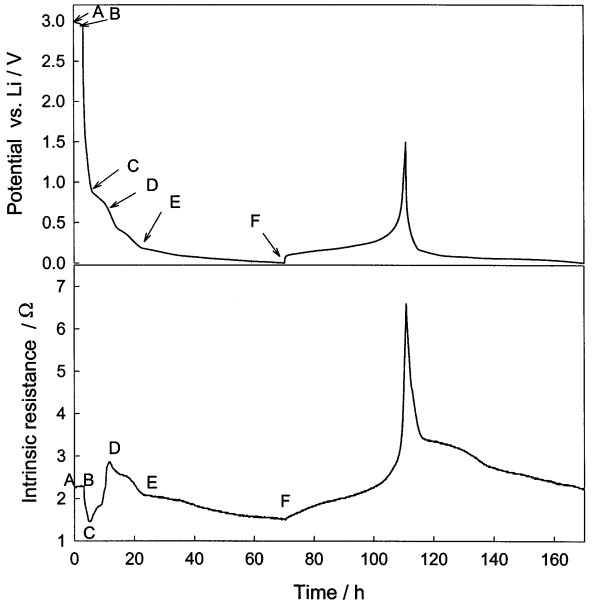

Fig. 2. Potential and intrinsic resistance of the KS 15 electrode during the first lithium insertion–extraction and second lithium insertion cycles. Charge–discharge current: 2.8 mA g^{-1}. Current for measuring intrinsic resistance: 5 mA.

2.3. EIS measurement

This was measured over a frequency range of 65 kHz to 1.0 mHz at a potentiostatic signal amplitude of 5 mV using a Solartron PRA 1250 frequency response analyzer with a Solartron Model 1286 electrochemical interface after electrodes were left at open circuit for 90 min for potential stabilization. For electrochemical reaction rate measurements, the signal was applied to the current collectors on both sides of the electrode. For intrinsic resistance measurement at high frequency, the EIS was measured between the two sides.

2.4. GIT measurements

Lithium was inserted and extracted to or from the electrode by the use of a series of current pulses of equal duration (1.0 h), such that the overall time required to pass 372 mA h g^{-1} was 72 h (C/72 rate). Following each pulse, the cell was left on open circuit for a time long enough to ensure equilibrium, yet short enough to prevent loss of lithium by self-discharge. The time chosen was 1.5 h. Meanwhile, the potential was recorded by computerized data acquisition. Depending on the electrode (see above), a constant 1 mA or 10 mA dc current was passed between the external current collectors to obtain the intrinsic resistance via the resulting voltage difference. The GIT charge–discharge current was lower than that used in Ref. [3], and the relaxation time was much longer. A low charge–discharge current of 0.25 mA (5.1 mA g^{-1}) was used to ensure a low overpotential (< 10 mV). This and the 1.0 h charge–discharge time ensured a uniform state of charge. Equally, the long open-circuit relaxation time ensured an equilibrium open-circuit potential. Hence, the lithium insertion–extraction reaction resistance at different lithium contents could be calculated directly from the ratio of overpotential to the charge–discharge current, and the electrode intrinsic resistance could be obtained with no interference from the charge–discharge current. An intrinsic resistance of 1.0 Ω could be measured quite accurately by application of 10 mA across the electrode. The experimental reaction resistance determined from the overpotential charge–discharge current slope should be the resistance of the electrolyte, the SEI film, the charge transfer reaction, lithium diffusion into graphite, together with any resistance associated with transfer between phases in the phase transformation region.

3. Results and discussion

3.1. In situ intrinsic resistance during initial cycling

Fig. 2 shows the potential and intrinsic resistance profile of KS 15 during the first charge–discharge and second charge cycles after allowing 3.0 h of immersion in the electrolyte for equilibration. The first charge curve has been subdivided into five sectors between initial state A and the five sharp discontinuities B-F. In the A-B zone, the electrode was at open-circuit for 3.0 h when the intrinsic resistance was about 2.2 Ω. SEI film formation is indicated by the increase in both the potential and the intrinsic resistance around 0.8 V (Fig. 3). The changes in these quantities at a lower charge current (1.25 mA g^{-1}) are shown for comparison.

On charge, the potential and intrinsic resistance both fell rapidly to $+0.85$ V and 1.3 Ω, respectively, in the B-C zone. Here lithium insertion occurs to form a dilute Stage 1 phase in which lithium is intercalated uniformly within the host, decreasing the potential [6], but increasing the conductivity of the host graphite [7] and reducing the intrinsic resistance. Simultaneously, formation of a small amount of SEI film on the surface occurs above $+0.8$ V [8,9]. The SEI film is permeable to Li^+ cations, but is electronically insulating, increasing the intrinsic resistance. The combined effect of the two opposing processes is first to reduce the rate of decrease of the intrinsic resistance, then to increase it starting at C (Fig. 3). When KS 15 was charged further, the potential fell from $+0.8$ to $+0.2$ V (zones C-D-E). Here, the principal reaction has been considered to be SEI formation (zone C-D) and solvated lithium intercalation (zone D-E) [10]. The plateau potentials at ca. $+0.4$ V in D-E may be explained as stages in the formation of solvated graphite intercalation com-

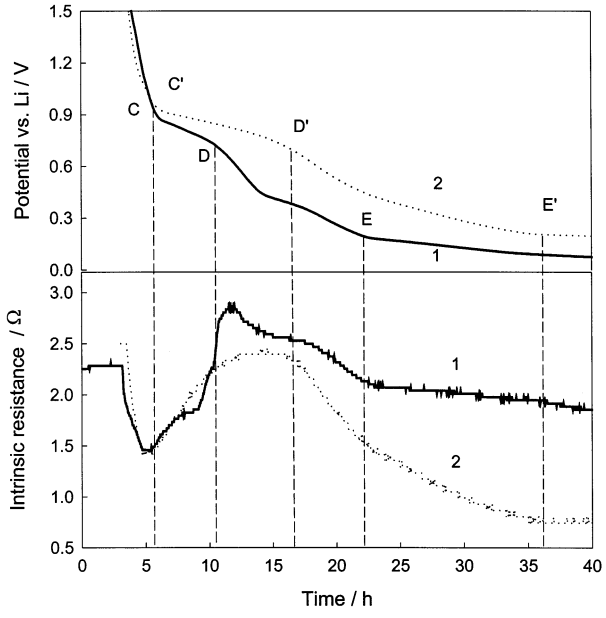

Fig. 3. Potential and intrinsic resistance of a KS 15 electrode during SEI film formation on the graphite surface. (1) Charge current: 2.8 mA g^{-1}. (2) Charge current: 1.25 mA g^{-1}. Current for intrinsic resistance measurement: 5 mA.

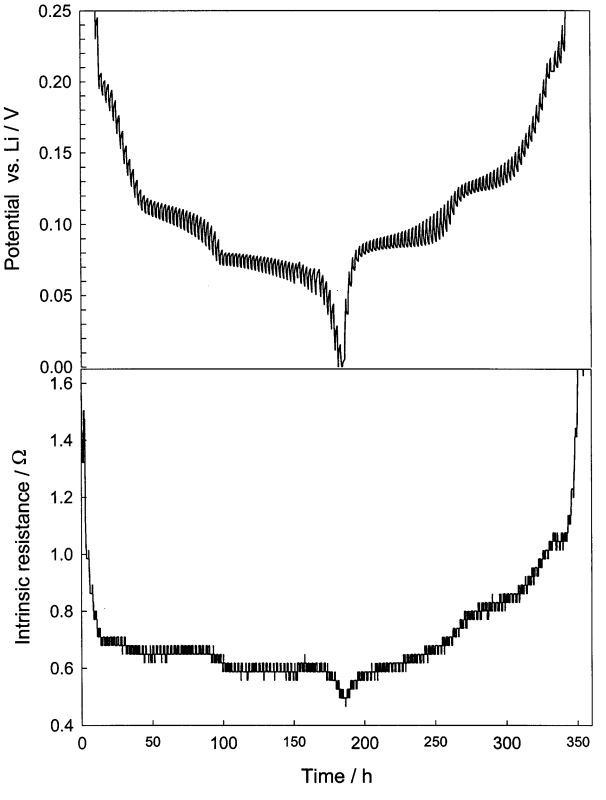

Fig. 4. Potential and intrinsic resistance as a function of time for the sixth cycle of a JM 287 electrode from galvanostatic intermittent titration via applied microcurrent pulses (GIT) technique. Charge–discharge current: 5.1 mA g^{-1}. The current pulse was imposed for 1.0 h then switched off for 1.5 h. Current for intrinsic resistance measurement: 10 mA.

pounds [10]. Fig. 3 shows that the rapid increase in intrinsic resistance in the C-D plateau is due to the formation of SEI film. The resistance reaches a maximum after D because the film continues to grow at the high charge current density used (2.8 mA g^{-1}). On decreasing the charge current density to 1.25 mA g^{-1} (Fig. 3, dashed line), the intrinsic resistance reached a maximum value at point D′, and the potential plateau in D-E disappeared. Comparison of the capacities in the C-D and D-E zones shows that the irreversible faradaic capacity of the SEI film in C-D is ca. 14 mA h g^{-1} for 2.8 and 1.25 mA g^{-1} charge currents. However, a large faradaic capacity difference (8.4 mA h g^{-1}) appears in D-E. This result indicates that a high lithium intercalation current has little effect on the SEI film in the C-D zone, but results in solvated lithium intercalation in the D-E zone. At high charge currents, the higher intrinsic resistance at E may be associated with solvated lithium intercalation.

In zone E-F in Fig. 2, the principal reaction is the reversible formation of the next step of the binary (per C_6 unit) lithium graphite insertion compound (GIC), Li_xC_6. These steps are represented by potential plateaus; those at ca. $+0.2$, $+0.1$, and $+0.08$ V have been assigned to phase transitions between dilute Stage 1 and Stage 4, Stage 2L and Stage 2, and Stage 2 and Stage 1, respectively [6]. In this zone the changes in intrinsic resistance and potential go in parallel, i.e. in successive discharge/charge cycles, both the intrinsic resistance and the potential changed in a similar manner, although the resistance showed an independent increase in Cycle 2 (Fig. 2). The intrinsic resistance and the potential of JM 287 and MCMB 10-28 behaved similarly to those of KS 15, although the increases with charge–discharge cycle number varied with each type of graphite. Since the intrinsic resistance is calculated from the voltage difference across the electrode, the potential of the side of the electrode receiving the charge–discharge current might influence measurements. This was eliminated by superposing GIT on the charge–discharge cycles when the intrinsic resistance was calculated from the voltage between the two sides of the electrode with a small current imposed at open circuit (see below).

3.2. GIT

Fig. 4 shows the potential and intrinsic resistance measured by applying a current signal across the electrode for JM 287 Cycle 6 obtained under GIT conditions as a function of time. The charge–discharge current pulse of 5.1 mA g^{-1} (0.255 mA for a 50 mg electrode) had little influence on the intrinsic resistance measurement, with an error not exceeding 6%. The overpotential gradually increased in the phase transformation region, but rapidly decreased in the single phase

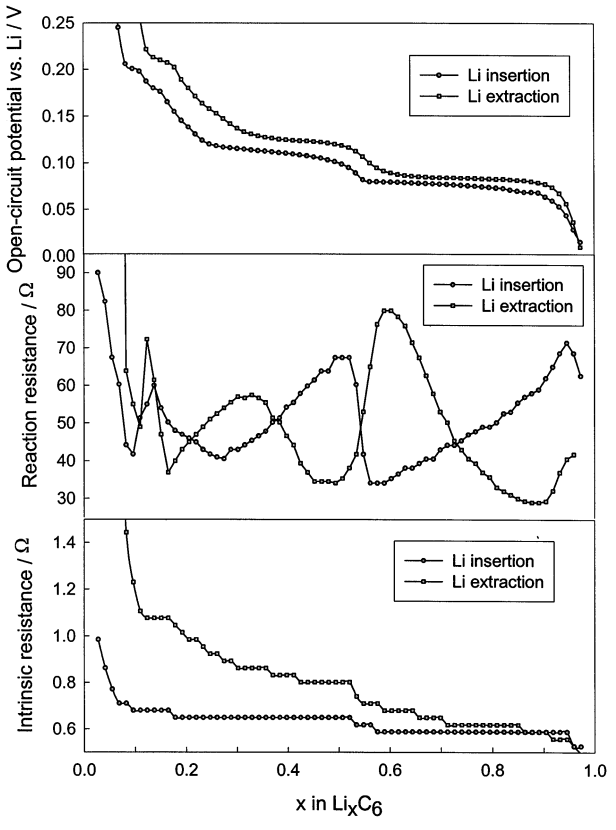

Fig. 5. Dependence of the open-circuit potential, intrinsic resistance and reaction resistance of JM 287 on lithium content. Before measurement, the electrode was cycled six times. Current for intrinsic resistance measurement: 10 mA.

region, while the intrinsic resistance slowly decreased during lithium insertion but rapidly increased during lithium extraction. The open circuit potential, reaction resistance and intrinsic resistance at different lithium insertion–extraction contents are shown in Fig. 5.

About 20 mA h g^{-1} (0.054 Li/C_6) of irreversible faradaic capacity with 10 mV of hysteresis in the potential had appeared by Cycle 6. This irreversible loss may result from lithium self-discharge over the long charge–discharge and relaxation times, or from continued SEI film growth, since the intrinsic resistance on charge was higher than on discharge. Hysteresis in the potential between charge and discharge may be related to expansion of graphite spacing on phase transformation [11].

The electrochemical reaction resistance on both charge and discharge gradually increased in the three-phase transformation region (the potential plateau), but fell to its original value in the single phase region. Lithium charging appears first to involve partially-solvated ion diffusion through the SEI film, electron transfer on the graphite surface, then lithium diffusion into graphite, followed by phase transformation. At small overpotentials, the charge transfer and lithium diffusion resistances may be linearized as RT/nFI_o and RT/nFI_L, respectively [12], where I_o and I_L are the exchange and lithium diffusion currents, respectively. The reaction resistance measured via dc pulses (Fig. 5) should therefore be the total resistances of the four steps. Resistance changes in the electrolyte, and SEI film, and in charge transfer are small during charge/discharge process [13,14], so the changes observed must correspond to changes in lithium diffusion and phase transformation resistances in graphite.

The change in diffusion resistance during phase transformation may be explained by the 'shrinking unreacted core' model [15] (to be discussed later), which has satisfactorily explained potential-step chronoamperometry results [16]. The measured resistance parallels the potential change for lithium charge–discharge, with a small variation, then a rapid change in the phase transformation and single phase regions, respectively. A more rapid increase was observed during discharge with JM 287 and MCMB 10-28. The latter also showed a reaction resistance maximum at the end of the potential plateaus, with a gradual decrease in measured intrinsic resistance with decreasing potential (Fig. 6).

Intrinsic resistances of JM 287 and MCMB 10-28 at different open circuit potentials during Cycles 5 and 6 are shown in Fig. 7. Both graphites show similar behavior as a function of potential and cycle number, i.e. there is a slow decrease in intrinsic resistance on charge

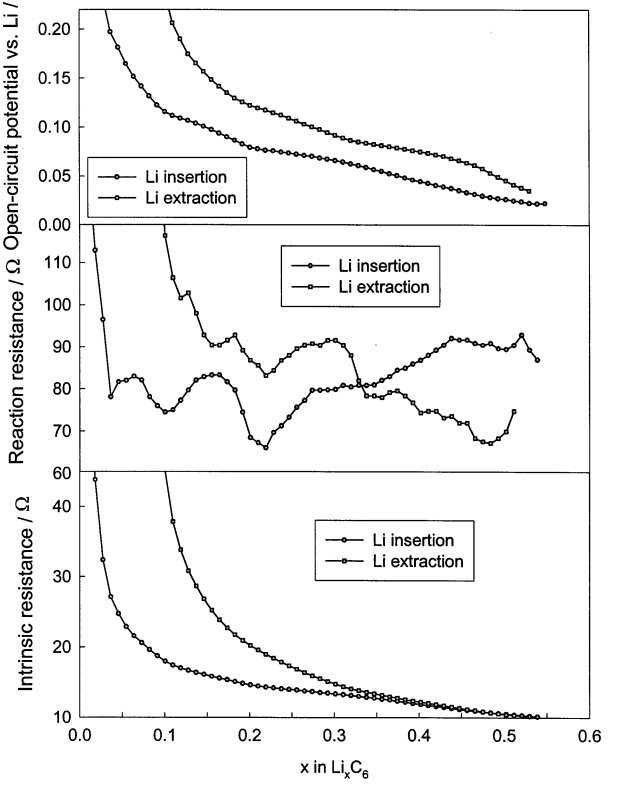

Fig. 6. Dependence of open-circuit potential, intrinsic resistance and reaction resistance of MCMB 10-28 on lithium content. Before measurement, the electrode was cycled for six times. Current for intrinsic resistance measurement: 1 mA.

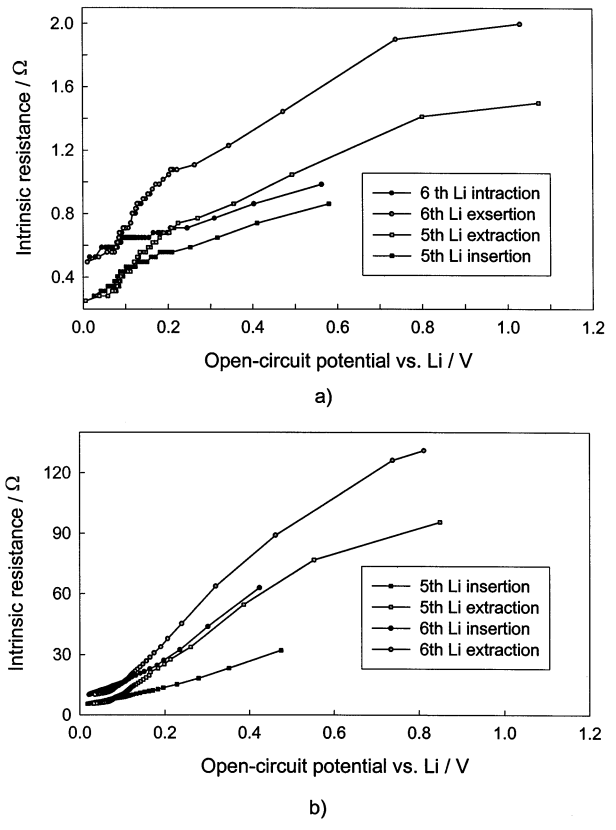

Fig. 7. Dependence of intrinsic resistance on open-circuit potential of graphite. (a) JM 287; (b) MCMB 10-28.

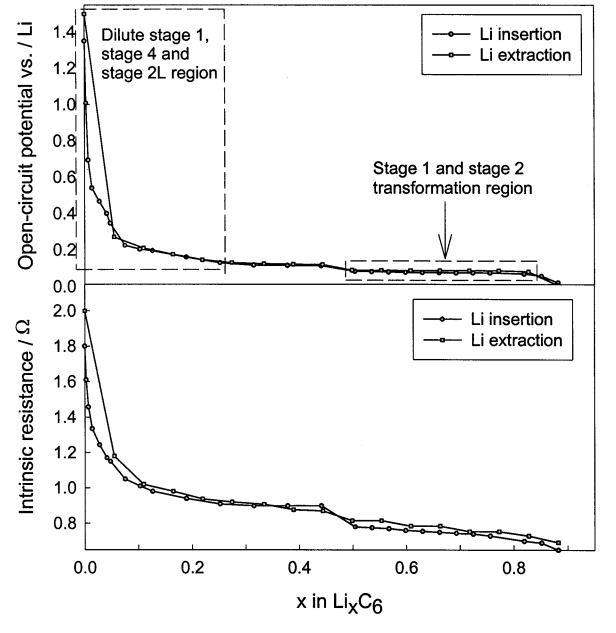

Fig. 8. Variation of open-circuit potential, intrinsic resistance of JM 287 during the ninth charge–discharge cycle. Circles: charge; Squares: discharge. EIS was used for intrinsic and reaction resistance measurement at each point.

below +0.2 V and a rapid increase during discharge above 0.1 V. Nishizawa et al. explain this by volume changes on charge and discharge [2], so a further increase should occur during phase transformation, where a large volume change takes place. However, a stable intrinsic resistance in this region is shown in the present results. Since the intrinsic resistance measured galvanostatically gives the total resistance, a more discriminatory technique such as EIS is required to investigate the contact resistance, which is part of the intrinsic resistance.

3.3. EIS measurement

JM 287 anodes were investigated to determine their reaction and intrinsic resistances as a function of lithium content. The latter were measured between the two sides of the electrode. Fig. 8 shows the open-circuit potential and instrinsic resistance during Cycle 9 (which were almost identical on charge and discharge) measured using 5.1 mA g^{-1} current pulses as for Cycle 6 in Fig. 5. The points indicate where the reaction resistance and intrinsic resistance were measured by EIS in the single phase region (dilute Stage 1, Stage 4, 2L) and in the phase transformation region (between Stage 1 and Stage 2). By Cycle 9s, the capacity and intrinsic resistance during charge and discharge were almost identical. Since the total charge–discharge times vary greatly with lithium content, and self-discharge may occur at long times, accurate reaction resistances at high lithium content were difficult to obtain. However, reaction resistances for JM 287 in the charge cycles 5–7 were very similar (Fig. 9), despite the capacity loss on cycling, i.e. reaction kinetics on this graphite are relatively invariant and capacity-independent, although the intrinsic resistance showed an increase in these cycles (Fig. 7).

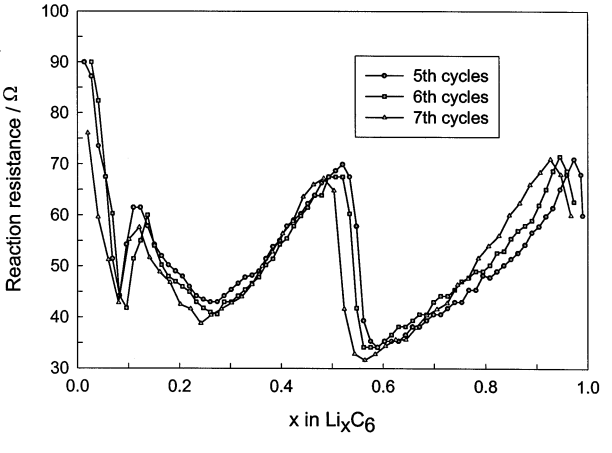

Fig. 9. Reaction resistance profile of JM 287 anode during Cycles 5–7. Applied current pulse: 5.1 mA g^{-1} for 1.0 h, followed by relaxation for 1.5 h.

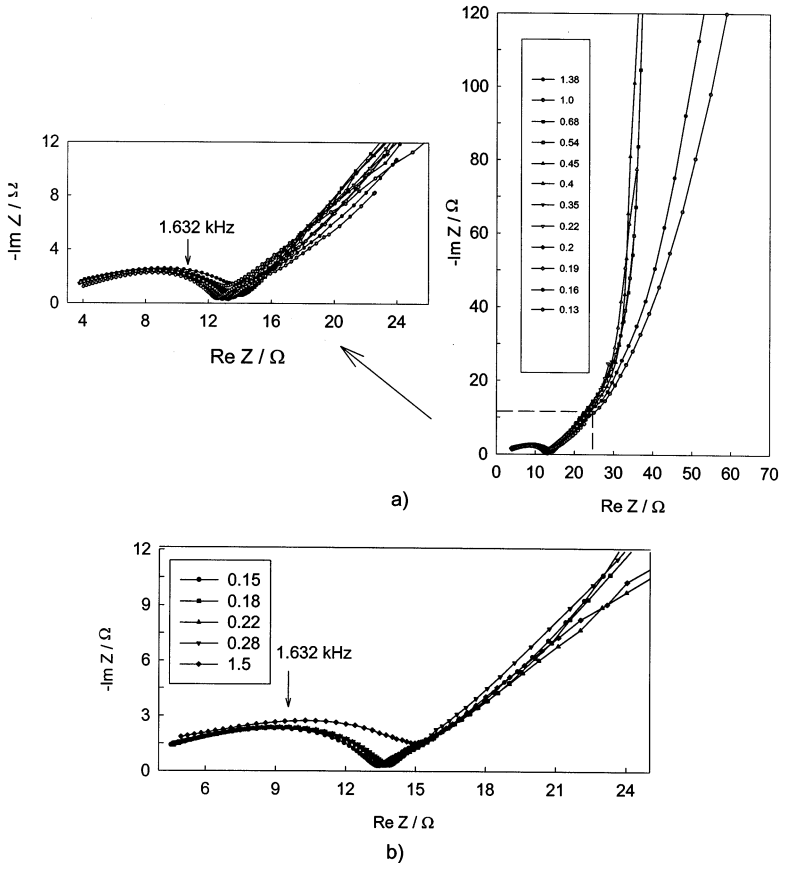

Fig. 10. Nyquist plots for (a) charge and (b) discharge kinetics into JM 287 in the potential range +1.5 to +0.13 V.

3.4. EIS in the single-phase region (dilute stage 1, and stages 2L, 4)

Fig. 10(a, b) show the differences of the electrochemical reaction impedance spectra between charge–discharge for JM 287 between +1.5 and +0.13 V. At high potentials a depressed high-frequency semicircle occurs along with a low-frequency positive slope, which becomes very steep at the lowest frequencies (Fig. 10(a)). The former may be attributed to the SEI film impedance and the latter to lithium diffusion [13]. On charge a further charge transfer semicircle is overlapped by the inclined lithium diffusion line at high potentials, but starts to appear at potentials below +0.2 V, and becomes clearer below 0.1 V (Fig. 13). Increase in the real part of the high-frequency semicircle between charge and discharge indicate some SEI film growth during Cycle 9. At high potentials (+1.38 V), the EIS for intrinsic impedance measurement shows two semicircles whose real resistances decrease with potential and become almost zero below +0.2 V (Fig. 11).

The intersection of the high-frequency line with the real axis decreases rapidly with decreasing potential. The two semicircles (see above) gradually become an inductive-resistive reactance as the potential is reduced from +2.3 to +0.13 V. On JM 287 and MCMB 10-28 graphites, the appearance of the inductive reactance depends on the intrinsic resistance, not on the potential. For example, it appeared in Cycle 1 for MCMB 10-28 when the intrinsic resistance increased from 1.6 to 0.2 Ω, but disappeared in Cycle 6 when the intrinsic resistance became greater than 10 Ω (Fig. 6). That the inductive reactance is an instrumental artifact is shown by EIS measured on the Solatron electrochemical interface terminals CE plus RE_1 and WE plus RE_2 connected together, or on an EIS of nickel wire, where the intercept to the real axis is the wire resistance. Hence, the intersection of the high-frequency line with the real axis in Fig. 11 must be the electronic resistance of the graphite electrode. Such artifacts are rather frequent, and may be avoided (when so identified) by omitting high frequency data. The two semicircles in Fig. 11 may be due to the contact impedance between the current collector to graphite powder, and graphite to graphite powder, respectively, which result from the SEI film giving incomplete particle contact after the volume change on cycling. For example, the electronic resistance of the graphite electrode decreased with increasing lithium content in dilute Stage 1 and Stage 2L (Fig. 11). Similar resistance changes have been noted in other dilute alkali metal graphite compounds (for example, C_xK, Rb, Cs) [7].

The contact resistance between graphite and the current collectors decreases progressively, and almost disappears at potentials below +0.2 V due to the almost continuous expansion of lithiated graphite in the single phase region between +1.5 and +0.13 V [6]. The soft SEI film must thereby be compressed or pushed aside, as scanning electron microscope observations suggest [17], showing its apparent disappearance by compression onto graphite fiber at low potentials, reappearing again on discharge to +2.5 V [16]. The appearance of the two semicircles in the plot for intrinsic impedance (Fig. 11(b)) may therefore be associated with shrinkage

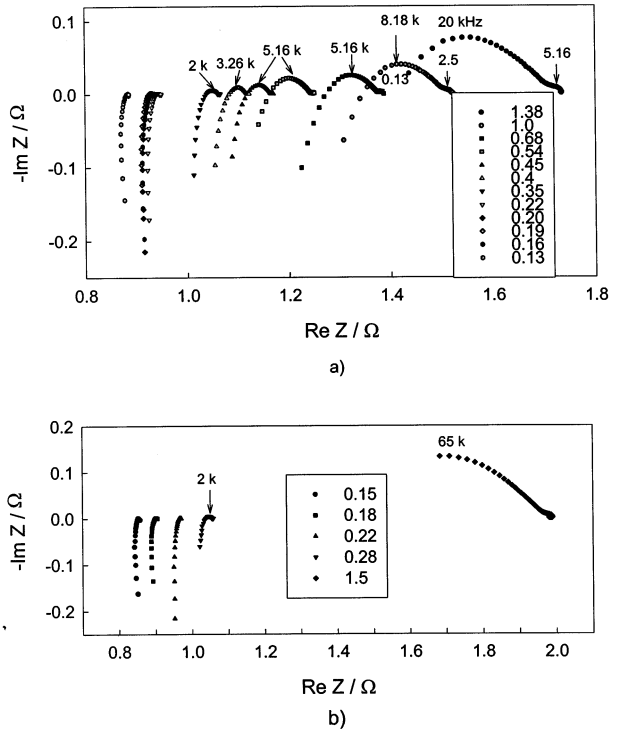

Fig. 11. Nyquist plots for intrinsic resistance of JM 287 in the potential range +1.5 to +0.13 V. (a) Charge; (b) discharge.

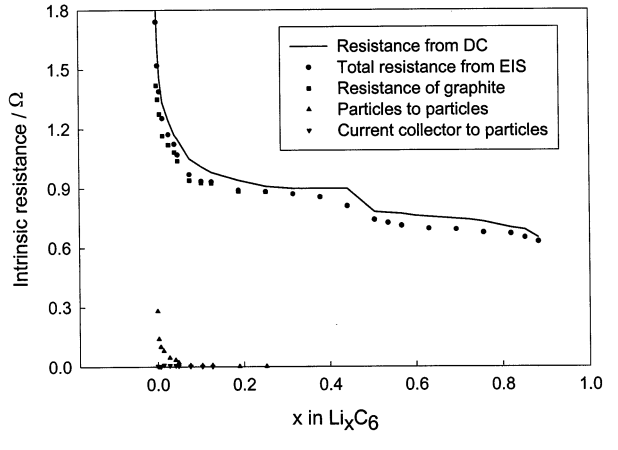

Fig. 12. Dependence of intrinsic resistance on graphite lithium content using dc and EIS methods.

of the discharging graphite and increasing SEI film thickness. If this is so, the SEI film must contain solvent under normal conditions.

The EIS plots show further SEI film growth on cycling, since the SEI film resistance increases from 6 Ω in the Cycle 1 to 10 Ω in Cycle 6. Intrinsic resistances measured from in situ dc signals (Fig. 8) and from EIS are compared in Fig. 12, which shows good agreement, EIS giving somewhat lower values. Thus the simple in situ method developed is of considerable practical value.

3.5. EIS in the stage transformation region (stage 1 to stage 2)

Fig. 13(a, b) shows the JM 287 electrochemical reaction impedance in the Stage 2 to 1 region and in the reverse transformation. Only a very small changes in SEI film and charge–transfer resistance were observed during stage transformation. However, a large change in the low-frequency lithium diffusion line is observed. Theoretical EIS analysis for lithium diffusion into spherical particles with phase transformation shows that a low-frequency semicircle should occur [4].

The large low-frequency imaginary part indicates a high diffusion resistance. Diffusion becomes slower as phase transformation progresses, whether the phase transformation is from Stage 1 to 2 or the contrary (Fig. 13). These EIS results are in good agreement with the GIT reaction resistance changes (Fig. 5). EIS spectra in Fig. 13 are similar to EIS plots obtained in the stage transformation region [18]. In contrast to the diffusion resistance, the intrinsic resistance remains almost the same between charge and discharge between Stages 1 and 2 (Fig. 14). Its EIS had no obvious semicircle, so changes must reflect those of graphite. The continuous decrease from Stage 1 to 2 and the increase in the other direction were due to the phase change, since the conductivity of Stage 1 is twice as high as that of Stage 2 [7].

3.6. Electrochemical kinetics during phase transformation

The total electrolyte, SEI film, and charge transfer resistance was ca. 18 Ω (Fig. 13), but the reaction resistance (without diffusion) from GIT was ca. 30 Ω (Fig. 5). The 12 Ω difference is evidently the phase transformation resistance, since GIT data should include it. To verify this, the GIT potential-time profile at the Stage 2 to 1 transformation (Fig. 4) was evaluated by examining the relaxation from the overpotential at each stage of charge and the corresponding equilibrium potential (Fig. 15). In all cases, a rapid relaxation of about 5 mV is initially observed, which is followed by a slow relaxation whose potential increases with the frac-

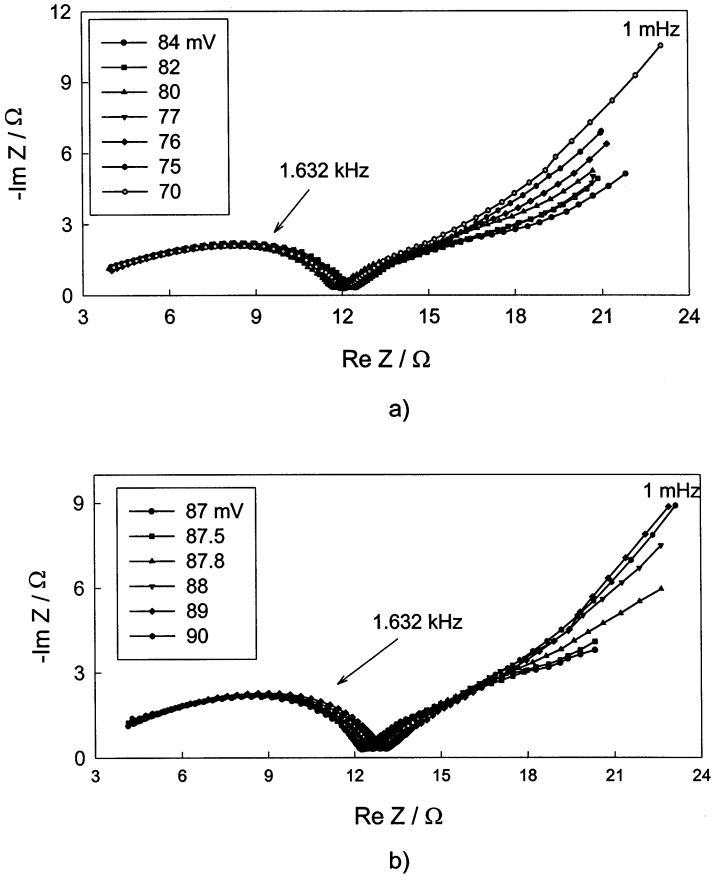

Fig. 13. Nyquist plots for charge–discharge kinetics into JM 287 in the phase transformation region. (a) From Stage 2 to 1; (b) from Stage 1 to 2.

tion of Stage 1 phase. The rapid change corresponds to the voltage drop for total electrolyte, SEI film and charge transfer reaction resistances, whereas the subsequent change may be attributed to phase transformation and lithium diffusion resistances. The former was ca. 20 Ω (i.e. 5 mV/0.25 mA), close to the 18 Ω determined by EIS (Fig. 13). The charge current pulse overpotential behaved correspondingly, as would be expected. The overpotential of the first charging pulse was stable after 0.5 h, but the region of stability shortened and finally disappeared in the following pulses as phase transformation progressed. A stable overpotential in the initial stage indicates that the phase transformation resistance is higher than that for lithium diffusion (discussed below).

Phase transformation may be explained by a shrinking unreacted core model (Fig. 16). During the initial charging, the lithium concentration gradually increases at the graphite plane edges, giving a slow overpotential increase. When the edge concentration exceeds the maximum Stage 2 supersaturation (equivalent here to 0.25 mA charge for 0.5 h), the Stage 1 phase nucleates from supersaturated Stage 2 phase, rapidly forming a continuous sheet. The stable overpotential indicates that lithium diffusion showed no concentration polarization for 0.5 h because of the short lithium diffusion distance, which permitted the phase boundary to move towards the particle center. The initial overpotential largely results from the growth of the Stage 1 phase from Stage 2, but the lithium concentration polarization slowly increases as the phase boundary moves toward the particle center and the diffusion length increases. The shrinking unreacted core model assumes that the phase transformation resistance is constant and the lithium diffusion resistance is proportional to $-\ln(1-X)$, where X is the fraction of the second phase (see Appendix). Thus:

$$R_{21} = \frac{RTr_o}{F^2 c_{12}}\left(\frac{2\pi}{k_{21}(c_{12}-c_{21})} - \frac{1}{D_i}\ln\sqrt{(1-X)}\right) \quad (1)$$

from Stage 2 to 1

$$R_{12} = \frac{RTr_o}{F^2 c_{21}}\left(\frac{2\pi}{k_{12}(c_{12}-c_{21})} - \frac{1}{D_2}\ln\sqrt{1-X}\right) \quad (2)$$

from Stage 1 to 2

where c_{12} and c_{21} are the lithium concentrations of the Stage 1 phase in equilibrium with Stage 2 and of the Stage 2 phase in equilibrium with Stage 1, D_1 and D_2

are the lithium diffusion coefficients in Stages 1 and 2, and k_{12}, k_{21} are the rate constants for phase transformation from Stage 1 to 2 and from 2 to 1, respectively. r_o is the average graphite particle radius. The constant resistance of stage transformation (first terms on the right side of Eqs. (1) and (2)) and gradual increasing resistance of lithium diffusion (second terms) are in agreement with the interpretation that increase of reaction resistance during phase transformation (Fig. 5) is due to lithium diffusion. Fig. 17 plots diffusion resistance in the between Stage 1 to 2 as a function of $-\ln(1-X)$, showing an approximately linear relationship for the forward and backward transformation. The higher slope for the first compared with that for the second is because $c_{12} > c_{21}$ (Eqs. (1) and (2)). Even though it supposes cylindrical symmetry with the diffusion and phase transformations in a steady state, the experimental resistances are in satisfactory agreement with the model. A small negative experimental deviation in the high lithium content may result from the short relaxation time (1.5 h) used, which may not be enough to achieve equilibrium.

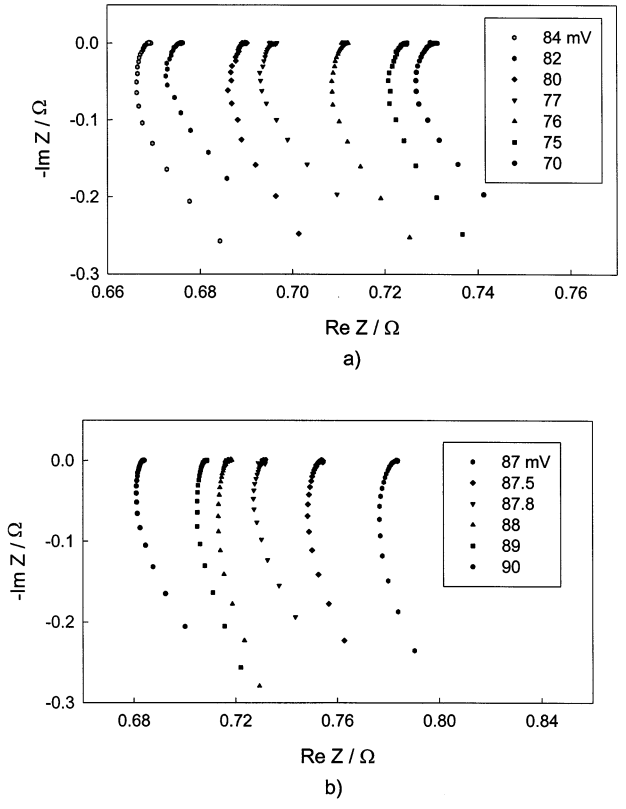

Fig. 14. Nyquist plots for intrinsic resistance of JM 287 in the phase transformation region. (a) From Stage 2 to 1; (b) from Stage 1 to 2.

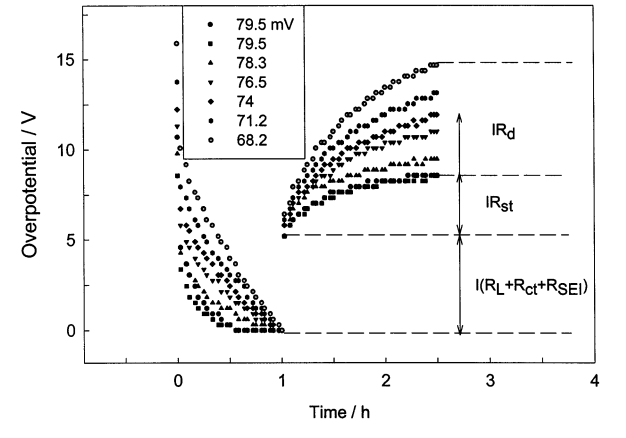

Fig. 15. Overpotential relaxation-time profile for JM 287 at different stages of phase transformation from Stage 2 to 1 using GIT. The final overpotential at the end of each lithium insertion step is put equal to zero, and the relaxation potentials are measured from this value. R_L, R_{ct}, R_{SEI}, R_{st}, and R_d are the electrolyte, charge transfer, SEI film, Stage transformation and lithium-in-graphite diffusion resistances, respectively.

Overall, the resistances are as follows (Fig. 5[13]): stage transformation, 12 Ω > SEI film, 10 Ω > charge transfer, 6 Ω > electrolyte 2 Ω. The diffusion resistance changes from 0 to 31 Ω as the Stage 1 fraction increases. When it exceeds 0.52, the diffusion resistance becomes greater than 12 Ω, so the rate-determining step then changes from phase transformation to lithium diffusion. Similar behavior was also reported by Pyun et al. [11] and Barsoukov et al. [20].

3.7. Electrochemical kinetics in the single-phase region

The high reaction resistance at the end of phase transformation becomes less in the single-phase region (Figs. 5 and 9). The reasons are not clear but the absence of a phase transformation resistance in this region, together with the decrease in the derivative of the open-circuit potential as a function of lithium content (dP_{oc}/dX), may be significant. The latter indicates that the same lithium composition gradient between the surface and center of a graphite particle will result in a lower overpotential at low dP_{oc}/dX.

EIS modeling based on the shrinking unreacted core concept predicts that the diffusion impedance should have the properties of a Warburg impedance in series with a capacitance in the high frequency region. Published results [13,19] show good agreement with these predictions. The dP_{oc}/dX value for the diffusion impedance Z_w should be the slope of the potential versus lithium composition in a single phase outside of the phase transformation region, as Fig. 16 indicates. By regarding dP_{oc}/dX as an unknown during fitting of experimental impedance spectra for MCMB graphite as a function of degree of intercalation, Barsoukov et al. [20] found that the best fit dP_{oc}/dX value is higher than that measured from potential-composition curves in the phase transformation region, but is similar to it in the single phase region, which confirms the present predictions. In almost all diffusion coefficient measurements derived from EIS plots in the phase transformation

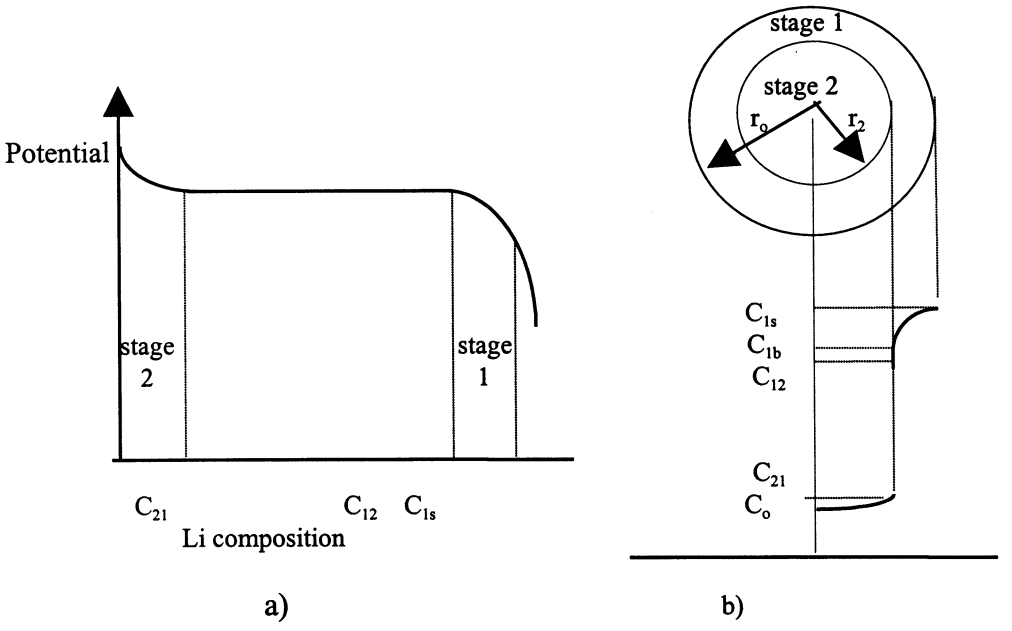

Fig. 16. (a) Equilibrium potential vs. lithium composition in the phase transformation region between Stage 2 and 1. (b) Schematic concentration profiles during stage transformation from Stage 2 to 1.

region, a dP_{oc}/dX value has been selected to calculate the lithium diffusion coefficient in the host material [13,19,21], which results in an apparent large change in lithium diffusion coefficient during phase transformation. Because the fitting accuracy in this region is low, Takami et al. have chosen to use an equation containing no dP_{oc}/dX term to calculate the lithium diffusion coefficient [22].

4. Conclusions

In situ intrinsic resistance measurements and microperturbation techniques such as GIT via applied microcurrent pulses and EIS have been applied to investigate the charge–discharge behavior over time and the kinetics of the lithium-insertion graphite anodes. The regions of rising intrinsic resistance observed in in situ resistance versus lithium composition curves at around + 0.8 V s. Li/Li^+ result from SEI film formation on the graphite host material. EIS of JM 287 graphite shows that the intrinsic resistance depends largely on the conductivity of lithiated graphite at potentials below + 0.2 V, but the parts attributed to contact resistance between the current collector and graphite, and between graphite particles, appeared at potentials above + 0.2 V. The increase in contact resistance above + 0.2 V is presumably caused by the volume change during lithium insertion–extraction and the increase in thickness of the SEI film.

GIT with microcurrent pulsing shows that the reaction resistance increases in the three-stage transformation region, and then relaxes in the following single phase region. EIS measurement indicates that the increase in reaction resistance in the stage transformation region results from the gradual increase in lithium diffusion path length. Phase transformation and lithium diffusion in graphite may be satisfactorily described by the shrinking unreacted shrinking core model, which can satisfactorily explain charge–discharge kinetics in this system. From the EIS and GIT measurements, we conclude that the electrochemical reaction for lithium insertion into JM 287 graphite in the phase transformation region is initially determined by the rate of phase change, and thereafter is controlled by the diffusion of lithium in the new phase.

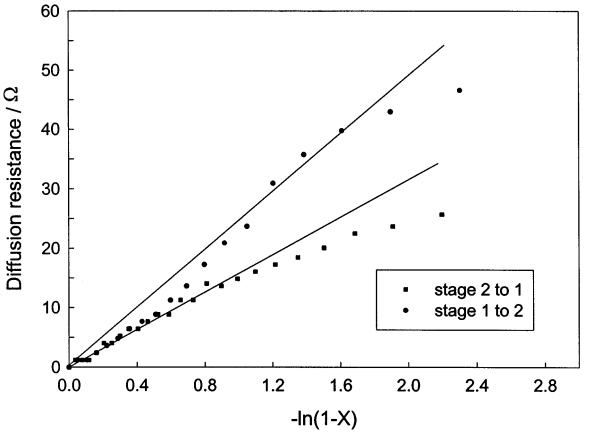

Fig. 17. The variation of diffusion resistance of JM 287 with $\ln(1 - X)$ during stage transformation between Stages 1 and 2.

This work shows that a high reaction resistance may decrease in the single phase region. From the kinetic viewpoint, an effective candidate anode material should undergo several phase transformations during charge and discharge.

Acknowledgements

We gratefully acknowledge NASA-Glenn Research Center, Cleveland, OH, for support of this work.

Appendix A. Resistance lithium diffusion resistance in graphite with cylindrical symmetry

Reaction resistance in phase transformation from Stage 2 to 1: It is generally accepted that lithium ions intercalate predominantly into graphite from the edge plane, and then diffuse inside in a direction parallel to the basal plane. JM 287 has been subjected to some mechanical milling. SEM images show that it has a circular cross section with a diameter of about 15 μm. JM 287 particles may therefore be considered to be cylindrical in using the shrinking unreacted core model to describe the phase boundary moving toward to the particle center (Fig. 16). A further simplification assumes steady-state charge–discharge.

From Fick's first law, and lithium flux continuity in Stage 1, the following equation may be obtained:

$$2\pi rFD_1\frac{dc_1}{dr}=2\pi r_oFD_1\frac{dc_1}{dr}\bigg|_{r=r_o}=2\pi r_oI_c \tag{A1}$$

where F is the Faraday constant, r_o the average graphite particle radius, I_c the cathodic current density, and D_1 is the diffusion coefficient for lithium in the Stage 1 phase, which is taken to be constant. Integrating Eq. (A1) with the boundary conditions $r=r_o,\ c_1=c_{1s},\ r=r_2,\ c_1=c_{1b}$:

$$c_{1s}=c_{1b}-\frac{I_cr_o}{FD_1}\ln\frac{r_2}{r_o} \tag{A2}$$

where r_2 is the radius of the unreacted Stage 2 material and c_{1b} is the lithium concentration in Stage 1 at the boundary with Stage 2. The fraction of Stage 1 transformed can be expressed as $X=V_{stage1}/V=1-(r_2/r_o)^2$, therefore Eq. (A2) can be rewritten as:

$$c_{1s}=c_{1b}-\frac{I_cr_o}{FD_1}\ln\sqrt{1-X} \tag{A3}$$

If the transformed Stage 1 is incoherent with Stage 2, the transformation rate of Stage 1 is [23]:

$$\frac{dV_{stage\ 1}}{dt}=k_{21}(c_{1b}-c_{12}) \tag{A4}$$

where c_{12} is the lithium concentration of Stage 1 equilibrated with Stage 2, and k_{21} is the rate constant for stage transformation. From mass conservation at the boundary between the Stage 1 and 2 phases:

$$F(c_{1b}-c_{21})\frac{dV_{stage\ 1}}{dt}=2\pi FD_1\frac{dc_1}{dr}=2\pi r_oI_c \tag{A5}$$

where c_{21} is the lithium concentration at the equilibrium Stage 2/Stage 1 boundary. Combining Eqs. (A4) and (A5), we obtain:

$$c_{1b}=c_{12}+\frac{2\pi r_oI_c}{Fk_{21}(c_{1b}-c_{21})} \tag{A6}$$

Substituting Eq. (A6) into Eq. (A3), then:

$$c_{1s}=c_{12}+\frac{2\pi r_oI_c}{Fk_{21}(c_{1b}-c_{21})}-\frac{I_cr_o}{FD_1}\ln\sqrt{1-X} \tag{A7}$$

Because the phase transformation resistance is small (12 Ω), $c_{1b}\approx c_{12}\gg c_{21}$ hence Eq. (A7) may be rewritten as:

$$c_{1s}=c_{12}+\frac{2\pi r_oI_c}{Fk_{21}(c_{12}-c_{21})}-\frac{I_cr_o}{FD_1}\ln\sqrt{1-X} \tag{A8}$$

The overpotential due to the phase transformation from Stage 2 to 1 and lithium diffusion is:

$$\eta_{21}=\frac{RT}{F}\ln\frac{c_{1s}}{c_{12}}=25.6\ln\left(1-\frac{c_{12}-c_{1s}}{c_{12}}\right) \tag{A9}$$

When the charge–discharge current is low, the overpotential is small. At $\eta<10$ mV, Eq. (A9) can be linearized:

$$\eta_{21}=\frac{RT}{F}\ln\frac{c_{1s}}{c_{12}}=\frac{RT}{F}\frac{c_{1s}-c_{12}}{c_{12}} \tag{A10}$$

Substituting Eq. (A8) into Eq. (A10), the resistance due to lithium diffusion into the host and phase transformation from Stage 2 to 1 can be obtained:

$$R_{21}=\frac{RTr_o}{F^2c_{12}}\left(\frac{2\pi}{k_{21}(c_{12}-c_{21})}-\frac{1}{D_1}\ln\sqrt{1-X}\right) \tag{A11}$$

Reaction resistance in phase transformation from stage 1 to 2: the overpotential in phase transformation from Stage 1 to 2 (cf. Eq. (A11)) can be expressed as:

$$R_{12}=\frac{RTr_o}{F^2c_{21}}\left(\frac{2\pi}{k_{12}(c_{12}-c_{21})}-\frac{1}{D_2}\ln\sqrt{1-X}\right) \tag{A12}$$

where I_d is the lithium extraction current, D_2 is the lithium diffusion coefficient in Stage 2, and k_{12} is the corresponding rate constant. The first term on the right side of Eqs. (A11) and (A12) indicates the resistances of the stage transformation are constant. The second terms, which reflect the lithium diffusion resistances, are proportional to $\ln(1-x)$.

References

[1] E. Peled, J. Electrochem. Soc. 126 (1979) 2047.
[2] M. Nishizawa, H. Koshika, I. Uchida, J. Phys. Chem. B 103 (1999) 192.
[3] A.H. Whitehead, M. Perkins, J.R. Owen, J. Electrochem. Soc. 144 (1997) L93.
[4] C.S. Wang, J. Electrochem. Soc. 145 (1801) 1998.
[5] C.S. Wang, I. Kakwan, A.J. Appleby, F.E. Little, J. Electrochem. Soc., in press.
[6] J.R. Dahn, Phys. Rev. B 44 (1991) 9170.
[7] M.S. Dresselhaus, G. Dresselhaus, Adv. Phys. 30 (1981) 139.
[8] K.A. Hirasawa, T. Sato, H. Asahina, S. Yamaguchi, S. Mori, J. Electrochem. Soc. 144 (1997) L81.
[9] A.C. Chu, J.Y. Josefowicz, G.C. Farrington, J. Electrochem. Soc. 144 (1997) 4161.
[10] M. Winter, P. Novak, A. Monnier, J. Electrochem. Soc. 145 (1998) 428.
[11] S.-I. Pyun, Y.-G. Ryu, J. Power Sources 70 (1998) 34.
[12] A.J. Bard, L.R. Faulkner, Electrochemical Methods: Fundamentals and Applications, Wiley, New York, 1980.
[13] A. Funabiki, M. Inaba, Z. Ogumi, S.I. Yuasa, J. Ostuji, A. Tasaka, J. Electrochem. Soc. 145 (1998) 172.
[14] T. Piao, S.-M. Park, C.-H. Doh, S.-I. Moon, J. Electrochem. Soc. 146 (1999) 2794.
[15] C.S. Wang, X.H. Wang, Y.Q. Lei, C.P. Chen, Q.D. Lei, J. Hydrogen Energy 21 (1996) 471.
[16] A. Funabiki, M. Inaba, T. Abe, Z. Ogumi, J. Electrochem. Soc. 146 (1999) 2443.
[17] K. Zaghib, K. Tatsumi, Y. Sawda, S. Higuchi, H. Abe, T. Ohsaki, J. Electrochem. Soc. 146 (1999) 2784.
[18] A. Metrot, A. Harrach, Electrochim. Acta 38 (1993) 2005.
[19] M.D. Levi, D. Aurbach, J. Phys. Chem. B 101 (1997) 4630.
[20] E. Barsoukov, J.H. Kim, J.H. Kim, C.O. Yoon, H. Lee, Solid State Ionics 116 (1999) 249.
[21] E. Barsoukov, J.H. Kim, J.H. Kim, C.O. Yoon, H. Lee, J. Electrochem. Soc. 145 (1998) 27.
[22] N. Takami, A. Satoh, M. Hara, T. Ohsaki, J. Electrochem. Soc. 142 (1995) 371.
[23] D.A. Porter, Phase Transformation in Metals and Alloys, Van Nostrand Reinhold, New York, 1981.